Reviews in Mineralogy & Geochemistry
Vol. 58, pp. 181-203, 2005

^{4}He/^{3}He Thermochronometry: Theory, Practice, and Potential Complications

David L. Shuster and Kenneth A. Farley

Division of Geological and Planetary Sciences
California Institute of Technology
Pasadena, California, 91125, U.S.A.
dshuster@caltech.edu farley@gps.caltech.edu

INTRODUCTION

Thermochronometry most often involves the determination of a cooling age from parent and daughter abundances within an entire crystal or population of crystals (Dodson 1973). Complementary information exists in the spatial concentration distribution of the daughter, $C(x,y,z)$, within a single crystal. By combining a bulk cooling age with $C(x,y,z)$ on the same sample, it is possible to place tight limits on the sample's time-temperature (t-T) path. Techniques for this kind of analysis have been developed for several different parent/daughter systems including U-Th-Pb and K-Ar (Harrison et al. 2005). Here we describe how this approach is applied to the (U-Th)/He system. The particular attraction of the (U-Th)/He method is its sensitivity to uniquely low temperatures. For example, the nominal ^{4}He closure temperatures (at 10 °C/Myr) for apatite, zircon and titanite are 70 °C, 180 °C, and 200 °C, respectively (Reiners and Farley 1999, 2001; Farley 2000; Reiners et al. 2002, 2004). In the case of apatite, we will show that significant diffusive mobility of ^{4}He occurs at temperatures just slightly higher than those of the Earth's surface. In this chapter, we present an overview of the *^{4}He/^{3}He thermochronometry* technique in which the natural spatial distribution of ^{4}He is constrained by stepwise degassing ^{4}He/^{3}He analysis of a sample containing synthetic, proton-induced ^{3}He. We present the fundamental theory, assumptions, practical aspects of proton irradiation and stepwise ^{4}He/^{3}He analyses, as well as several example applications of ^{4}He/^{3}He thermochronometry.

In particular, we illustrate how the ^{4}He/^{3}He technique can be used to determine the helium diffusion kinetics *and* constrain the natural ^{4}He distribution within an individual crystal or a small population of crystals, and how this information can be used to constrain the sample's t-T path. We also discuss some of the complications that have arisen and summarize the current state of research on this new thermochronometer.

FUNDAMENTAL CONSIDERATIONS

The basic principles and assumptions of (U-Th)/He dating have been described in detail elsewhere (Farley 2002). Here we concentrate only on aspects particular to the ^{4}He/^{3}He variant of the method. Like other radio-thermochronometers, (U-Th)/He dating involves two physical processes: radiogenic ingrowth of a daughter product (^{4}He) and thermally activated volume diffusion of the daughter. However, a difference between the (U-Th)/He system and other chronometers is that multiple parent nuclides produce a common daughter through α decay. Although α decay of ^{147}Sm also produces ^{4}He, the vast majority of radiogenic ^{4}He in minerals is produced via actinide decay. Once in a state of secular equilibrium, the actinide decay series

1529-6466/05/0058-0007$05.00 DOI: 10.2138/rmg.2005.58.7

emit 8, 7, and 6 α-particles for a single decay of ^{238}U, ^{235}U and ^{232}Th, respectively. The ^{4}He ingrowth equation can therefore be written:

$$^{4}\mathrm{He} = 8 \cdot {}^{238}\mathrm{U} \cdot \left(e^{\lambda_{238} t} - 1\right) + 7 \cdot \left(\frac{^{238}\mathrm{U}}{137.88}\right) \cdot \left(e^{\lambda_{235} t} - 1\right) + 6 \cdot {}^{232}\mathrm{Th} \cdot \left(e^{\lambda_{232} t} - 1\right)$$

where ^{4}He, ^{238}U and ^{232}Th indicate present-day abundances, t is the accumulation time or He age, λ is a radioactive decay constant ($\lambda_{238} = 1.511 \times 10^{-10}$ yr^{-1}, $\lambda_{235} = 9.849 \times 10^{-10}$ yr^{-1}, $\lambda_{232} = 4.948 \times 10^{-11}$ yr^{-1}), and (1/137.88) is the present day ^{235}U/^{238}U ratio.

The ^{4}He spatial distribution

The basis for ^{4}He/^{3}He thermochronometry is that the spatial distribution of radiogenic ^{4}He within a U and Th bearing crystal is an evolving function of the sample's *t-T* path. This can be summarized by the following schematic equation which applies to an individual crystal:

$$\int_{t_o}^{today} \left[Production(x,y,z,t) - Removal(x,y,z,T,t) \right] dt = Distribution(x,y,z,today)$$

where *Production* is the time dependant radiogenic production function of ^{4}He, *Removal* is the time and temperature dependent diffusive loss function, *Distribution* is the spatial concentration function of ^{4}He within the sample today, and t_o is the time when ^{4}He accumulation initiates. With knowledge of these functions, the above expression provides a relationship between measurable quantities and the desired *t-T* path of the sample. Since the physics which describes and relates these functions is well established, the challenge is to quantify the functional form of each. ^{4}He/^{3}He thermochronometry provides an analytical technique to constrain (1) the *Distribution* function in a sample today and (2) the *Removal* function (i.e., via the helium diffusion kinetics). For a sample with uniformly distributed parent nuclides, the standard assumptions of (U-Th)/He dating provides (3) the *Production* function through knowledge of the bulk U and Th concentrations in the sample today. Although non-uniform parent distributions could easily be incorporated into the theory, for simplicity we initially consider only the uniform case.

Classical diffusion theory provides the necessary relationships between time, temperature and the spatial distribution of a radiogenic noble gas within a solid matrix (Carslaw and Jaeger 1959; Crank 1975). Using numerical methods, the classical theory can be extended to any arbitrary geometry. However, specific analytic solutions to the production – diffusion equation exist. The spherical solution is the most useful, and one which provides the clearest way to illustrate and conceptualize the relationship between t, T and $C(x,y,z)$ within a crystal. For the purposes of this chapter, we focus on the spherical solution, and discuss below why the spherical model is useful for many geological applications.

Within a spherical diffusion domain, and for known diffusivity (D), the radial concentration distribution of a diffusing substance can be described along a single spatial dimension r, ($0 \le r \le a$). For an initial radial concentration distribution $C_0(r)$ and assuming no ingrowth, the concentration at a later time is given by:

$$C(r,\tau) = \frac{2}{ar} \sum_{k=1}^{\infty} e^{-k^2\pi^2\tau} \sin\left(\frac{k\pi r}{a}\right) \int_0^a r' C_o(r') \sin\left(\frac{k\pi r'}{a}\right) dr' \qquad (1)$$

(Carslaw and Jaeger 1959) if its mobility follows volume diffusion and $C_0(a) = 0$ for all t. Here, we use the non-dimensional diffusion time

$$\tau(T,t) = \int_0^t \frac{D(T,t')}{a^2} \cdot dt' \tag{2}$$

and assume that diffusion is thermally activated. These relationships provide a mechanism by which to compute the ^{4}He distribution along any arbitrary *t*-*T* path. By discretization of τ_i to be a piecewise linear quantity

$$\tau_i = \tau(T_i, t_i) \tag{3}$$

the radial distribution after a discrete step of duration t_i at T_i is given by

$$C_i(r) = C(r, \tau_i) \tag{4}$$

These expressions are useful for predicting the evolution of a radial ^{4}He profile within a spherical diffusion domain over geologic time. Along a discretized *t*-*T* path, the profile evolution is calculated by first adding a finite "dose" of radiogenic ^{4}He, then diffusively evolving the profile according to Equation (4). Because individual crystals of the minerals commonly used for (U-Th)/He dating [apatite (Farley 2000; Reiners and Farley 2001), titanite (Reiners and Farley 1999), zircon (Reiners et al. 2002)] act essentially as single diffusion domains, we consider the effect of thermal history on the ^{4}He distribution within a single diffusion domain rather than a distribution of domains.

To illustrate the above expressions, Figure 1 shows ^{4}He profiles obtained after eight different *t*-*T* paths assuming helium diffusion kinetics equivalent to those of Durango apatite (Farley 2000; Shuster and Farley 2004). We have chosen to use the Durango apatite He diffusion kinetics throughout this chapter because they are amongst the best determined of all minerals, and because they demonstrate the low temperature sensitivity available from the apatite ^{4}He/^{3}He method. Shown in Figure 1a,d are cooling histories; the resultant radial ^{4}He distributions are shown in Figure 1b,e. The first simulation (Fig. 1a,b) ended when the temperature reached 25 °C whereas the second simulation (Fig. 1d,e) was followed by late stage isothermal accumulation at 25 °C for 5 Myr. Note that these simulations assume temperature only varies with time, and does not vary across the diffusion domain.

Figure 1 shows that slow cooling and prolonged residence at elevated temperatures yields low concentrations of ^{4}He near the domain edge. In contrast to these "rounded" profiles, those generated by rapid cooling or a long duration at low temperatures where diffusion is very slow have higher concentrations near the edge, they are more "square." The point is that each of the eight distributions in Figure 1 distinctly reflects the *t*-*T* path on which it was produced. With knowledge of a sample's helium diffusion kinetics, model ^{4}He distributions can be calculated according to any arbitrary *t*-*T* path. Alternatively, if the natural ^{4}He spatial distribution within a sample can be constrained, then a finite set of *t*-*T* paths consistent with both the sample's ^{4}He distribution and He age can be identified.

Proton-induced ^{3}He

As Figure 1 illustrates, most of the difference among the ^{4}He profiles is found in the outermost few percent of the domain (e.g., $r/a > 0.90$). Because typical accessory minerals have dimensions of only ~100 μm, distinction among profiles like these (and thus *t*-*T* paths) requires a technique for ^{4}He detection that has a spatial resolution of better than a few microns. We are unaware of a technique by which to directly measure a ^{4}He concentration distribution at this resolution. Instead, we use a stepwise degassing approach that simultaneously yields both pieces of information we require: the ^{4}He concentration profile *and* the helium diffusion kinetics of the same sample. With only a single isotope (^{4}He) it is impossible to de-convolve the effects of a non-uniform ^{4}He distribution and unknown helium diffusivity from a set of

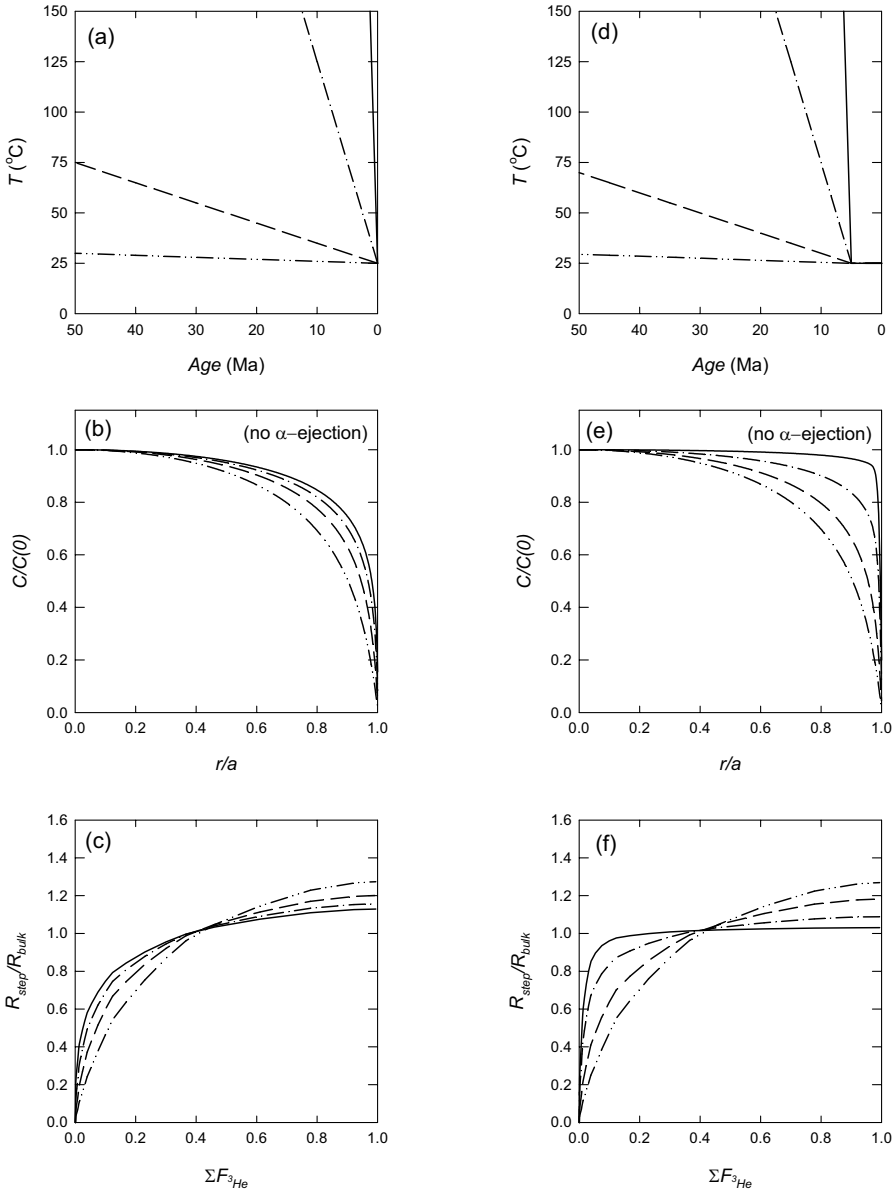

Figure 1. Simulated radial ^{4}He distributions and corresponding ^{4}He/^{3}He spectra resulting from monotonic cooling, modified from Shuster and Farley (2004). The concentration profiles shown in (b) and (e) result from the *t*-*T* paths shown in (a) and (d), respectively and the helium diffusion kinetics of Durango apatite and no isotopic fractionation. The resultant step-heating simulations are shown as ratio evolution diagrams in (c) and (f), respectively. Shown are the simulated isotope ratios for each release step, R_{step} (R=^{4}He/^{3}He), normalized to the bulk ratio R_{bulk} plotted vs. the cumulative ^{3}He release fraction, $\Sigma F_{^3He}$. The simulations excluded the effect of α-ejection.

helium release fractions (Shuster and Farley 2004). In 1969, Turner showed that the presence of a second, synthetically generated, and uniformly distribution Ar isotope (^{37}Ar or ^{39}Ar) is useful for constraining the distribution of radiogenic ^{40}Ar in a degassing experiment (Turner 1969). In 1978, Albarède showed how stepwise degassing Ar data can be used to directly invert for the ^{40}Ar distribution (Albarède 1978). The development of $^{4}He/^{3}He$ thermochronometry has largely been based on these results. Step-heating of a sample that contains a uniform distribution of ^{3}He solves this difficulty: ^{3}He release fractions quantify helium diffusion kinetics, while evolution of the $^{4}He/^{3}He$ ratio over the course of sequential degassing constrains the natural radiogenic helium profile.

Shuster et al. (2004) demonstrated that sufficient ^{3}He for this application can be generated within minerals via energetic proton irradiation. The ^{3}He nuclei are produced from all atoms in the mineral as spallation products of nuclear reactions initiated by the incident protons. The experiments of Shuster et al. (2004) showed that (i) lattice damage associated with proton irradiation does not affect the helium diffusion properties of at least apatite and titanite, (ii) the proton-induced distribution of ^{3}He is uniform, (iii) diffusion parameters determined from ^{3}He are in excellent agreement with those determined from ^{4}He for both apatite and titanite, (iv) the technique produces ^{4}He at levels orders of magnitude lower than are found in minerals of interest for He dating, and (v) the sample is heated by less than a few °C during irradiation, so helium diffusion during the process is negligible.

A uniform ^{3}He distribution is useful for two reasons: (i) it enables a stepwise degassing experiment in which the ^{4}He release fractions are normalized to the ^{3}He released in the same step; we illustrate below how this *ratio evolution experiment* constrains the natural ^{4}He distribution within the sample, and (ii) it satisfies the initial condition from which diffusion coefficients are easily calculated (Fechtig and Kalbitzer 1966).

Unlike ^{39}Ar, which is induced via neutrons reacting with ^{39}K and thus tracks the parent isotope ^{40}K, ^{3}He induced by energetic protons is not uniquely generated from the parent nuclides of radiogenic ^{4}He. Proton-induced ^{3}He is effectively generated from all atoms that are present in the irradiated mineral. Therefore, unlike the $^{40}Ar/^{39}Ar$ method, $^{4}He/^{3}He$ release data do not define a radiometric age for each step. However, if U and Th are uniformly distributed throughout a particular sample, then some of the features in the ratio evolution diagram carry age significance when combined with a bulk He age.

The $^{4}He/^{3}He$ ratio evolution diagram

Proton-induced ^{3}He provides a means to interrogate the natural ^{4}He distribution within a sample by sequentially measuring $^{4}He/^{3}He$ ratios during stepwise degassing. During a degassing experiment, the $^{4}He/^{3}He$ release spectrum or *ratio evolution diagram* is a sensitive function of the natural spatial distribution of ^{4}He (Shuster and Farley 2004). This diagram is a plot of the $^{4}He/^{3}He$ ratio in each step (R_{step}) normalized to the $^{4}He/^{3}He$ ratio of the bulk sample (R_{bulk}) as a function of cumulative ^{3}He release fraction, $\Sigma F_{^{3}He}$. In effect, each step "mines" deeper into the diffusion domain. We will show how forward model simulations can be compared against an observed ratio evolution diagram to constrain the ^{4}He distribution. Alternatively, Shuster and Farley (2004) described a linear inversion to directly solve for the unknown ^{4}He distribution from the $^{4}He/^{3}He$ spectrum.

The simulated radial distributions presented in Figure 1 can be used to illustrate the sensitivity that the $^{4}He/^{3}He$ ratio evolution diagram has for constraining spatial ^{4}He distributions. The same expressions used to model radiogenic ingrowth and diffusion in nature can also be used to model evolution of the ^{4}He and ^{3}He distributions during a degassing experiment. The only difference is that the radiogenic production is negligible over the timescale of an experiment.

For a given diffusion kinetics, $D(T)/a^2$, Equation (4) predicts the piecewise evolution of the radial distribution after discrete steps of duration t_i at T_i of a simulated degassing experiment for any arbitrary initial profile, $C_0(r)$. By integrating the profiles and taking their differences between each step, a set of simulated helium release fractions is calculated for any arbitrary heating schedule. And if the two helium isotopes have known relative diffusivity (see below), Equation (4) can be used to calculate isotope ratios for the concurrent release of a uniformly distributed isotope (^{3}He) and an isotope with an arbitrary natural distribution (^{4}He). This simulates a ^{4}He/^{3}He stepwise degassing experiment.

Figure 1(c,f) shows the simulated ratio evolution diagrams corresponding to each of the distributions shown in Figure 1(b,e), respectively. Here we assume that both helium isotopes have the same diffusivity, an issue which we consider more fully below. The important result is that the various profiles yield easily measurable differences in isotopic ratio (up to factors of a few), especially in the initial few percent of ^{3}He release (i.e., the helium derived from near the domain edge).

The effect of α-ejection

One complication unique to the (U-Th)/He method is that α particles are emitted with sufficient energy that they travel ~20 microns from the site of decay, and some fraction are ejected from grain surfaces. In the case of commonly dated minerals like apatite, titanite, and zircon, the edge of the diffusion domain corresponds to the α-ejection boundary. This effect exerts a strong and predictable spatial effect on the ^{4}He production function that is independent of diffusion (Farley et al. 1996), particularly in smaller grains.

Although α-ejection influences the ^{4}He distribution, Shuster and Farley (2004) demonstrated that if the effect is incorporated into the modeling, it does not significantly diminish the sensitivity of ^{4}He/^{3}He thermochronometry. Figure 2 illustrates the consequences of α-ejection on a ^{4}He profile and its corresponding ^{4}He/^{3}He ratio evolution diagram. This profile was generated by assuming the production function consistent with an α-particle range of 20 microns (see Eqn. 1 of Farley et al. 1996). Shown in Figure 2a is the radial distribution within a 65 μm (radius) spherical domain that experienced 10 °C/Myr cooling and α-ejection. Shown for reference is the profile calculated for the same cooling rate, but without α-ejection. Alpha-ejection clips and flattens the ^{4}He distribution and

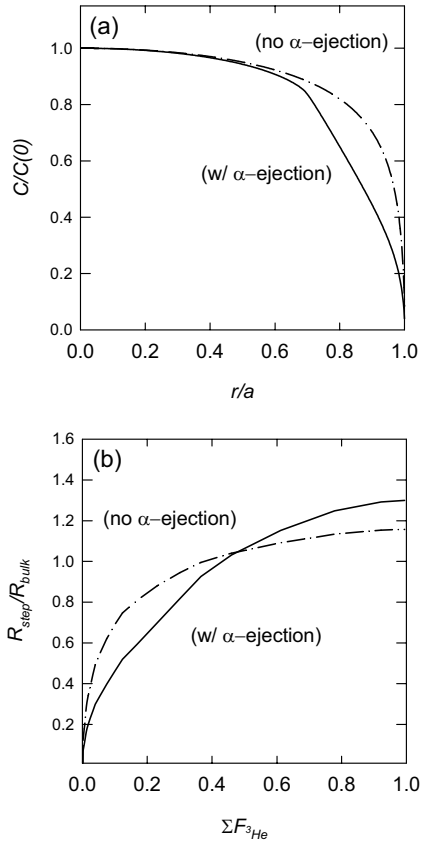

Figure 2. The α-ejection profile. Shown in (a) are two ^{4}He profiles calculated including (solid curve) and excluding (dash-dot curve) the effect of α-ejection, modified from Shuster and Farley (2004). The α-ejection profile was calculated for a spherical diffusion domain with 65 μm radius. These profiles both result from the same *t*-*T* path shown as a "dash-dot" curve in Figure 1a. Shown in (b) are the corresponding ratio evolution diagrams.

as shown in Figure 2b it also dramatically influences the ratio evolution diagram. The effect introduces a distinct linearity in the first ~30% of the ratio evolution diagram which cannot be ignored in interpretive models.

Note that the overall *shape* of a ratio evolution diagram is independent of the specific diffusion kinetics (i.e., $D(T)/a^2$) and heating schedule of a particular experiment. For a single diffusion domain, the shape of the diagram is controlled only by the initial spatial distribution of ^{4}He (a small potential effect of differences in diffusivity between the two isotopes is discussed below). Therefore, the ^{4}He spatial distribution can be determined *without* knowledge of the helium diffusion kinetics of a particular sample. However, to interpret the profile in terms of the *t-T* path by which it was produced requires knowledge of $D(T)/a^2$ for the helium in that specific sample.

The ^{3}He Arrhenius plot

Calculating diffusion coefficients from a stepwise degassing experiment requires specification of the initial spatial distribution, $C_0(x,y,z)$ of the diffusant (Fechtig and Kalbitzer 1966). Although an initially uniform concentration across a spherical diffusion domain, $C_0(r) = constant$, is typically assumed, this assumption is violated for samples that experienced ^{4}He loss by diffusion and/or α-ejection. Failure to incorporate an appropriately rounded or clipped distribution in the Fetchig and Kelbitzer (1969) computation will yield diffusivities that underestimate the true values, potentially by several orders of magnitude. Therefore, ^{4}He release fractions cannot in general be used to quantify helium diffusion kinetics in most natural samples, despite previous efforts to do so (Lippolt et al. 1994; Wolf et al. 1996; Warnock et al. 1997; Reiners et al. 2002). Laboratory generated ^{3}He, on the other hand, does not pose this problem because the induced distribution is uniform.

An important consideration for this method is whether proton-induced ^{3}He diffusivities are a reliable proxy for radiogenic ^{4}He. It is possible that the two isotopes are sited sufficiently differently that their diffusion behavior differs. In addition, there is a general expectation that the two isotopes will diffuse at slightly different rates given their substantial mass difference.

Shuster et al. (2004) demonstrated that to within analytical uncertainty the diffusion kinetics inferred from ^{3}He are equivalent to those based on radiogenic ^{4}He in Durango apatite and Fish Canyon tuff titanite. The apatite study was performed on an interior aliquot of this large gem quality apatite. Because the analyzed material was obtained at a distance from the α-ejection clipped edge, and because the apatite was quickly cooled it can be assumed to have a uniform distribution of radiogenic ^{4}He. (Note that the variability in He content inferred from the spatial variations in U and Th content reported by (Hodges and Boyce 2003) are far too small to influence this conclusion). In a more detailed study of Durango apatite, Shuster et al. (2004) also demonstrated that diffusive fractionation of helium isotopes can safely be neglected throughout a degassing experiment of that sample. These results indicate that proton-induced ^{3}He is an excellent proxy for ^{4}He in at least this apatite. Additional experiments on more typical apatites are more difficult to interpret because of probable rounding of the ^{4}He profile. In some of these samples diffusive fractionation may be present. Even if the diffusivities vary by the 15% predicted from their masses, a ^{3}He based Arrhenius plot would adequately describe ^{4}He diffusion kinetics for calculating He ages and concentration profiles on specified *t-T* paths. However, small diffusivity differences between the two isotopes *will* influence the shape of the ratio evolution diagram (see below).

An important advantage of ^{4}He/^{3}He thermochronometry over the conventional bulk age approach is that helium diffusion kinetics is determined for each analyzed sample. There is no need to extrapolate diffusion parameters to different grain sizes or to assume that a set of diffusion parameters measured on one sample apply to another sample.

Constraining thermal histories

In this section we consider how results of a ^{4}He/^{3}He experiment can be used to restrict a sample's allowable *t*-*T* paths. Three pieces of information are required: (i) the ^{4}He distribution, (ii) the function $D(T)/a^2$ for helium in the sample, and (iii) the bulk He age. In general a large number of thermal histories will be consistent with these three observations. Like other problems of this nature (e.g., see (Albarède 1978)), to determine a sample's actual thermal history from a measured spatial ^{4}He distribution is an ill posed problem (Shuster and Farley 2004); a unique solution is not generally possible.

In many ways this situation is analogous to attempts to constrain *t*-*T* paths from fission track length distributions (Gallagher 1995) and from multi-domain K-feldspar ^{40}Ar/^{39}Ar dating (Lovera et al. 1989). As with those techniques, one approach is to generate possible *t*-*T* paths, forward model the resulting observables, and minimize the mismatch to measurements. Ultimately, we believe this will be the most effective way to interpret ^{4}He/^{3}He data. Nevertheless, there are several approaches that allow a more intuitive interpretation of the data under certain circumstances.

^{4}He/^{3}He age spectra

In many thermochronometry studies the age of a discrete and relatively large magnitude cooling event is sought. For example, rocks may cool rapidly as a consequence of vertical motion on faults or due to river incision associated with surface uplift. The most common approach for dating these events is to obtain an age-elevation transect involving multiple samples (House et al. 1998; Stockli et al. 2000). Provided the event was of sufficient magnitude to cool rocks that were originally above their closure temperature, the age of the event can be determined. However, in cases where the event is of smaller magnitude or where vertical sampling is impractical, it can be difficult or impossible to date the event using a bulk age. The ^{4}He/^{3}He method provides an alternative and far more sensitive approach that can be performed on a single sample.

Figure 3 illustrates such an application. Consider a forward problem in which geologic evidence indicates a discrete rapid cooling event, arbitrarily assumed to be from 50 °C to 0 °C. If one obtained a (U-Th)/He age of, e.g., 5 Ma on an apatite with a = 65 μm, it would not be possible to determine when the cooling event occurred from this sample alone: all six cooling histories in Figure 3 would result in a 5 Ma bulk He age. However, each of the *t*-*T* paths yields a distinct ratio evolution diagram, especially for the ^{4}He/^{3}He ratio of the first gas released (e.g., at $\Sigma F_{^3\mathrm{He}} < 0.01$). The earlier the cooling event the higher the ^{4}He/^{3}He ratio in the first step, from zero for recent cooling up to the limit of ~ 0.55 dictated by α-ejection alone for the case of cooling at 5 Ma. The intuitive explanation is that prior to cooling, these samples were experiencing ^{4}He diffusion such that the edge of the grain was effectively at zero age. After rapid cooling and the cessation of diffusion, the edge of the grain began to quantitatively retain ^{4}He and "age."

This effect is analogous to the age significance in initially derived gas in a ^{40}Ar/^{39}Ar age spectrum (McDougall and Harrison 1999). However, an important difference between the Ar and He systems is the influence that α-ejection has upon the distribution. Note that the computations shown in Figure 3 included the effect of α-ejection. This phenomenon is not problematic for the technique, but it does need to be considered. When we account for α-ejection, the initially derived ^{4}He/^{3}He carries age significance at the limit that essentially no diffusion takes place after a fixed point in time, and as $\Sigma F_{^3\mathrm{He}} \rightarrow 0$. A second difference between the He and Ar based methods is the need to use the bulk He age to translate the ^{4}He/^{3}He ratio into a step age. This arises because ^{3}He is not directly correlated with the parent nuclides of ^{4}He.

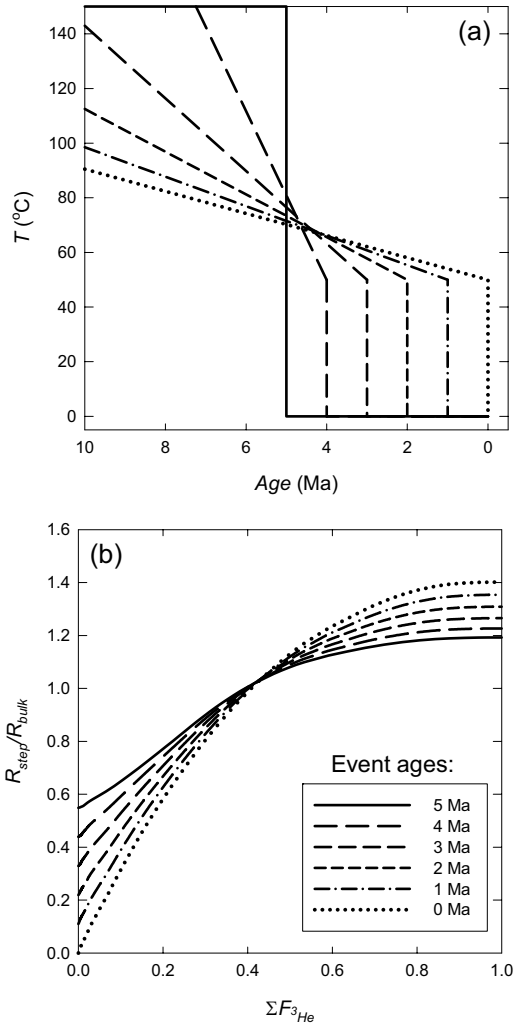

Figure 3. The edge effect. Shown in (a) are six *t-T* paths which each result in a bulk He age of 5 Ma. Their corresponding ^{4}He profiles (not shown) were calculated using Durango apatite helium diffusion kinetics including the effect of α-ejection. The ^{4}He profiles correspond to the six simulated ratio evolution spectra shown in (b).

On timescales less than ~100 Ma, a model "*Edge Age*" can be calculated simply as a linear scaling of the α-corrected He age ($HeAge_{cor}$) by the ratio of the observed initial ^{4}He/^{3}He ratio [i.e., $(R_{initial}/R_{bulk})_{measured}$] to that predicted for a profile that expected from α-ejection alone [i.e., $(R_{initial}/R_{bulk})_{\alpha\text{-}ref}$]:

$$"EdgeAge" = \frac{\left(\frac{R_{initial}}{R_{bulk}}\right)_{measured}}{\left(\frac{R_{initial}}{R_{bulk}}\right)_{\alpha - ref}} \cdot HeAge_{cor} \quad (5)$$

where

$$\left(\frac{R_{initial}}{R_{bulk}}\right)_{\alpha-ref} = \frac{F_{edge}}{F_T}\sqrt{\frac{D^{4He}}{D^{3He}}} \tag{6}$$

F_T is the α-ejection correction factor (Farley et al. 1996):

$$F_T = 1 - \frac{3S}{4a} + \frac{S^3}{16a^3} \tag{7}$$

and F_{edge} is given by:

$$F_{edge} = -\frac{1}{4}\frac{(S-2a)}{a} \tag{8}$$

F_{edge} represents the fraction of α-particles that are retained at the edge of a spherical domain of radius a, and S is the average stopping distance of α-particles along the U and Th decay series (~20 μm). Using these expressions and by extrapolating the curves shown in Figure 3b to $\Sigma F_{^3He} \rightarrow 0$, we find that the initially derived $^4He/^3He$ ratios correspond exactly to the ages of rapid cooling in each simulation. The D^{4He}/D^{3He} term accounts for any diffusive fractionation between the helium isotopes upon degassing (see below). In the above simulations, $D^{4He}/D^{3He} = 1$.

The previous example illustrates how a portion of the ratio evolution diagram can have direct age significance. This concept can be generalized to produce a $^4He/^3He$ age spectrum. Because proton-induced ^3He is uniformly distributed, the ^3He release fractions are a measure of the volume of material interrogated by each step. Hence the $^4He/^3He$ ratio of each step is proportional to the ^4He concentration in the interrogated volume. By knowing the ^4He production function within the grain assuming uniform U and Th, we can translate the $^4He/^3He$ ratio for each step into a step age. To make the results more readily interpretable the $^4He/^3He$ release spectrum can be converted into a model age spectrum as follows:

$$"StepAge" = \frac{\left(\frac{R_{step}}{R_{bulk}}\right)_{measured}}{\left(\frac{R_{step}}{R_{bulk}}\right)_{\alpha-ref}} \cdot HeAge \tag{9}$$

Here the "α *-ref*" ratio is taken from the ratio evolution diagram computed for a sample of the same grain size as that actually analyzed, but with a ^4He profile dictated solely by α-ejection (the formula for such a profile is given by (Farley et al. 1996)). The "*measured*" and "α *-ref*" ratios are evaluated at the same values of $\Sigma F_{^3He}$.

An example serves to illustrate how an age spectrum can be used to answer a common geologic question. As discussed by Stockli et al. (2000), a rapid cooling event, for example induced by normal faulting, may be recorded as a fossil helium partial retention zone in an age-elevation plot, where the age of the lower inflection point ("break-in-slope") indicates the age of onset of exhumation. This is illustrated in Figure 4a, which shows a model age-elevation pattern for apatites that experienced thermal quiescence (no cooling) for 55 Myr followed by a rapid exhumation event at 10 Ma. In this example the inflection point would only be revealed after ~3 km of exhumation (assuming a geothermal gradient of 20 °C/km); if only 2 km of exhumation occurred, the He ages would provide no insight to the age of the cooling event (see Fig. 4a, right hand axis). However, the concentration profiles of samples

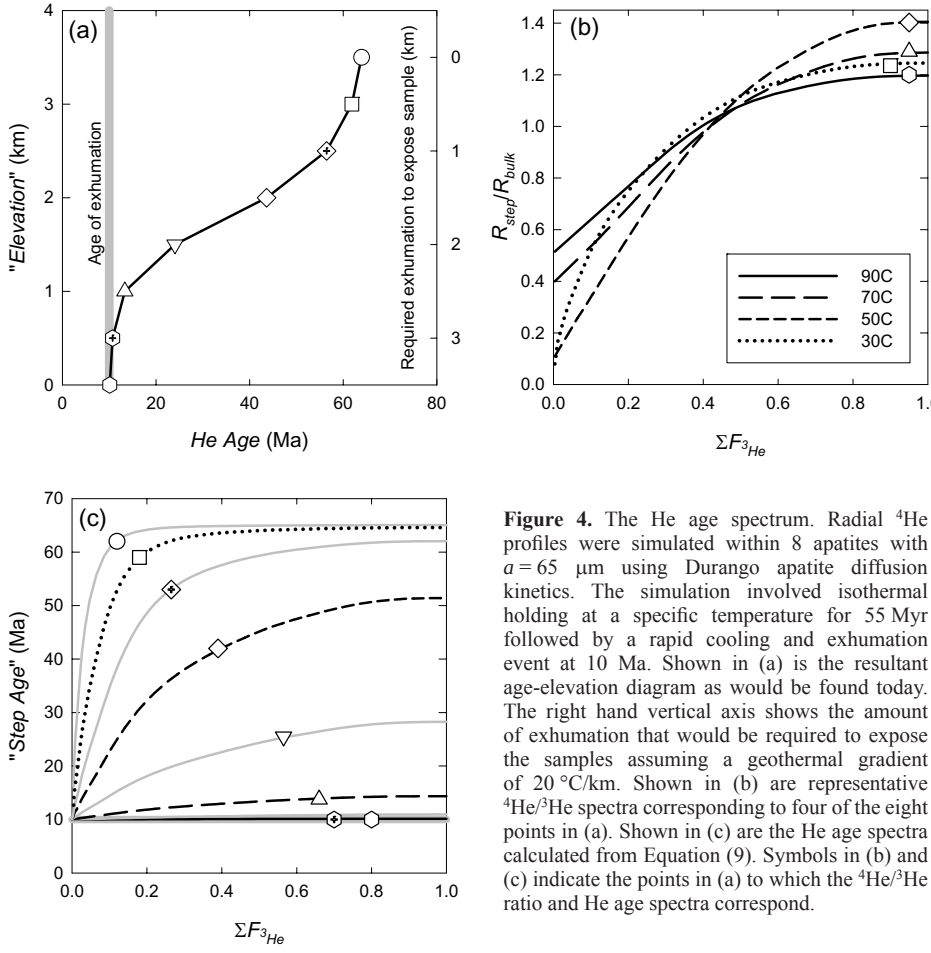

Figure 4. The He age spectrum. Radial ^4He profiles were simulated within 8 apatites with $a = 65$ μm using Durango apatite diffusion kinetics. The simulation involved isothermal holding at a specific temperature for 55 Myr followed by a rapid cooling and exhumation event at 10 Ma. Shown in (a) is the resultant age-elevation diagram as would be found today. The right hand vertical axis shows the amount of exhumation that would be required to expose the samples assuming a geothermal gradient of 20 °C/km. Shown in (b) are representative $^4He/^3He$ spectra corresponding to four of the eight points in (a). Shown in (c) are the He age spectra calculated from Equation (9). Symbols in (b) and (c) indicate the points in (a) to which the $^4He/^3He$ ratio and He age spectra correspond.

high up in the section carry the sought-for timing information, as well as information on their thermal state prior to exhumation. Shown in Figure 4b are the ratio evolution diagrams for 4 representative apatites at 0, 1, 2, and 3 km elevation. In the simulation, these samples resided at 90, 70, 50 and 30 °C, respectively, prior to exhumation.

Figure 4c shows model age spectra for all 8 apatites in this hypothetical sample suite. Each spectrum corresponds to a bulk He age and elevation as indicated by symbols in Figure 4a. As shown in Figure 3, every sample that was sufficiently hot to be diffusing significant He from the grain edge (i.e., above ~30 °C) will have an edge age approximating the age of exhumation. (In principle, the initial He released should be precisely the exhumation age, but in practice one must "mine deeper" into the profile to extract enough He to make the measurement).

The shape of the age spectrum at higher release fractions is also significant. For apatites coming from within the former ^4He partial retention zone (*HePRZ*; ~40–80 °C) the age spectrum is highly curved demonstrating long residence at temperatures where diffusive loss was rapid. Using numerical forward models it would be straightforward to distinguish samples generated in a thermally static *HePRZ* (this model) from, e.g., samples that migrated through the *HePRZ*

at some slow rate. More directly, steps from each of the structurally highest two samples achieve a plateau age of 65 Ma. This is because throughout the 65 Ma simulations these two samples were cool enough to quantitatively retain helium in the grain interior. From a practical perspective, such a plateau would demand that the sample had resided at low temperatures (e.g., <30 °C; a more quantitative estimate requires full modeling) for 65 Ma. This would set a limit on the paleodepth of this sample prior to exhumation, and hence an estimate of the total amount of exhumation that had occurred after 65 Ma. Thus by performing a ^{4}He/^{3}He analysis on one or several samples it would be possible to determine (i) the time at which a sample first cooled to temperatures where He is quantitatively retained in a grain interior (plateau age), (ii) the total amount of cooling and hence exhumation (from structural relationships involving a sample with a plateau age), (iii) the rate of cooling through the *HePRZ* (from the curvature of the age spectrum), and (iv) the age of onset of a rapid cooling event (from the edge age).

TECHNICAL ASPECTS

Proton irradiation

We have performed four proton irradiations: two at the Harvard Cyclotron Laboratory (now closed) using a 150 MeV proton beam, and two at the Northeast Proton Therapy Center (NPTC) with a 220 MeV beam. The NPTC generates a proton beam with a 4.5 m diameter cyclotron. In our latest irradiation, we generated 10^9 atoms ^{3}He/mg with a fluence of 1×10^{16} protons/cm^2 at 220 MeV, accomplished with a beam current of ~280 nA over a single 8 hour period. This is an enormous concentration of ^{3}He which easily permits single grain analyses.

Energetic proton irradiation produces spallation ^{3}He from nearly all target nuclei in the same way that cosmic rays produce ^{3}He in meteorites in space (Leya et al. 1998; Wieler 2002). Spallation ^{3}He is dominantly produced by a process known as charged particle evaporation. The initial interaction between the incident proton and a target nucleus can leave the residual target nucleus in an excited state, although most of the incident kinetic energy is likely carried off by a scattered nucleon. Upon de-excitation to a new ground state, the residual target nucleus has some probability of emitting a ^{3}He nucleus, e.g., ^{28}Si (p, p) ^{28}Si* $\rightarrow$ ^{25}Mg + ^{3}He. Because this process emits ^{3}He nuclei along stochastic trajectories at most probable energies between 1–10 MeV, we expect approximately isotropic ^{3}He distributions to be generated within the solid ~1 to ~50 μm surrounding each target atom in a mineral. For this reason the final siting of the ^{3}He nucleus should be crystallographically random and similar to that in which radiogenic ^{4}He resides after nuclear ejection. And since ^{3}He production probabilities are approximately equal from all target elements, the ^{3}He is *a priori* expected to be uniform. We believe that ^{3}He emission from grain edges will be approximately balanced by implantation from surrounding materials, so there is no equivalent to the α-ejection phenomenon with which to contend.

Spallation ^{4}He is produced along with ^{3}He, with a ^{4}He/^{3}He ratio of about 10. This amount of ^{4}He is negligible compared to the radiogenic ^{4}He in natural U and Th bearing minerals like apatite at least at the irradiation dosages we have used.

Cross sections for X(p,x)^{3}He reactions are strongly dependent upon proton energy below ~50 MeV, but remain relatively constant above ~100 MeV (Leya et al. 2000). Proton energies exceeding ~100 MeV will not substantially improve ^{3}He yields within a given sample. However because proton energy drops as the beam passes through solid matter, a higher beam energy does allow a thicker stack of samples to be irradiated. The range of protons through a target stack is directly proportional to the energy of the incident beam. To maximize the number of samples simultaneously irradiated, the target stack is constructed such that its length is near the overall range of protons. The range of 150 MeV protons is ~16 cm in Lucite

and ~7.5 cm in aluminum. At 220 MeV these ranges are ~34 and ~14.5 cm, respectively. In our latest irradiation, we irradiated ~100 samples at once. This number could easily be doubled while maintaining sufficient ^{3}He yield in each sample.

To generate a uniform ^{3}He distribution within a sample, a broad and defocused proton beam is required. This is achieved by first passing the incident beam through a 100 μm Pb foil prior to the samples. The Pb foil, as well as the target stack, causes a scattering of the protons causing the beam intensity profile (normal to the beam axis) to be approximately Gaussian in shape. For individual grains < 150 μm in radius, the resultant ^{3}He concentration distribution is uniform to within a few percent. This has been observationally verified in a crushed and sieved aliquot of ~180 μm Durango apatite (Shuster et al. 2004). Because the beam intensity varies by as much as 10% normal to its axis (along 15 mm diameter), for samples with diffusion domains >500 μm in radius, uniform ^{3}He production remains to be established. For such large samples the irradiation can be made more uniform by using a thicker scattering foil (at the expense of overall proton flux) or by continuously moving or spinning the sample relative to the beam.

When working with grains of a size typical of accessory minerals (<150 μm), the container within which the sample is held during the irradiation is critical. For each of the four irradiations, we experimented with a different type of sample container, and found the most success with small packets composed of two pieces of Sn foil cold welded together. Sn foil does not degrade under the high flux of protons, and the cold welded packets ensure quantitative recovery of all irradiated grains.

Sample requirements

The same sample requirements for conventional (U-Th)/He dating also apply for ^{4}He/^{3}He thermochronometry: euhedral crystals free of fluid and mineral inclusions. Since most information on the *t*-*T* path of a sample is contained toward the edge of the diffusion domain, it is of particular importance that the analyzed samples contain only original crystal surfaces (see Potential Complications).

As with conventional (U-Th)/He dating, the physical dimensions of each analyzed crystal need to be measured to determine the F_T value (Farley 2002). Since the degassing experiment provides the characteristic diffusive length scale "a" within the function $D(T)/a^2$, the F_T value is only relevant for simulating the effect of α-ejection. For an individual grain, a single F_T value relates the observed ratio evolution to spherical model calculations including α-ejection. However, for samples with low ^{4}He concentration, it has been necessary to run as many as 20 grains in a single degassing analysis. In such cases we have selected grains within a narrow size range, and calculated F_T values for each; the average F_T value for the population is then used in the model simulations. Because α-ejection adds uncertainty to both the ratio evolution diagram and the conventional age determination, it is desirable to analyze the largest possible grains.

Stepwise degassing analysis

For the reasons discussed above, the objective of a ^{4}He/^{3}He degassing experiment is two-fold: (i) to measure the ratio evolution diagram and (ii) to determine the function $D(T)/a^2$. These two objectives are not necessarily best achieved with the same heating schedule, so a compromise is required. For instance, a degassing experiment designed solely for the purpose of quantifying diffusion kinetics might incorporate multiple retrograde heating cycles (Farley 2000; Shuster and Farley 2004) and would not require steps at high cumulative helium yields. On the other hand, a well quantified ratio evolution diagram requires an even distribution of points across the budget of ^{3}He (i.e., on $0 < \Sigma F_{^3\mathrm{He}} < 1.0$). And, because retrograde degassing steps typically evolve small amounts of helium, they do not necessarily improve the quality of a ratio evolution diagram.

Our $^4He/^3He$ stepwise degassing analyses use the projector-lamp heating device (Farley et al. 1999) and a sector field noble gas mass spectrometer capable of resolving ^3He from HD (MAP 215-50). Because ^3He blanks are typically very low in this system, the ^3He detection limit does not limit the amount of irradiated material from being analyzed. A proton fluence of ~10^{16} p/cm^2 generates sufficient ^3He abundance that individual ~100 μm grains can be studied.

POTENTIAL COMPLICATIONS

Mineral surfaces

Analysis of samples with intact original surfaces is important because most of the thermal information contained in a concentration distribution is located toward the grain edges and because broken surfaces will generate misleading results in the stepwise degassing analysis. A broken surface (or a large crack) will expose a steeper concentration gradient than would otherwise exist in the sample. This would result in initially evolved $^4He/^3He$ ratios that are artificially too high. With careful sample selection, broken and/or cracked grains can be identified and avoided. Fortunately, in samples containing sufficient amounts of natural ^4He, the $^4He/^3He$ degassing analysis can be performed on very few or even single grains. The ^3He blank is sufficiently low that it is not usually the limiting factor in the $^4He/^3He$ analysis. While these are stringent criteria, we have been able to locate at least a few appropriate grains from the modest number of granitic apatite samples we have so far worked on.

Geometry

Throughout this chapter, we used the spherical diffusion domain as an analytically tractable model for actual diffusion domains. This model is clearly an oversimplification; in many cases euhedral (non-spherical) crystals act as the domains for ^4He diffusion (Reiners and Farley 1999, 2001; Farley 2000; Reiners et al. 2002). Although more elaborate calculations could be constructed to incorporate actual crystal geometry, the spherical domain is sufficient for the purposes of bulk (U-Th)/He thermochronometery (Meesters and Dunai 2002a,b). This conclusion applies to the $^4He/^3He$ method as well. For example, Shuster et al. (2004) illustrated that accurate spherical representations of diffusively modified ^4He distributions could be retrieved using $^4He/^3He$ release spectra from degassed Durango apatite despite the fact that the shards were non-spherical. In the case of a non-spherical domain, the Fechtig and Kalbitzer (1966) calculation effectively averages over the geometrically complicated nature of the material and returns a diffusion domain radius, a [i.e., $\ln(D/a^2)$], which on the average describes the characteristic diffusion length scale of the material and describes a sphere with a surface area to volume ratio approximating that of the actual domain.

However, for the above statements to be true, two conditions must be met. The first is that ^3He and ^4He release fractions are determined simultaneously. The ^3He $\ln(D/a^2)$ values and ^4He release fractions are specific to the diffusion domain geometry *and* experimental conditions during an analysis. Second, it is critically important that forward-calculated thermal models use the function $D(T)/a^2$ that is specific to the sample. The experimentally determined diffusivity, D, *and* the characteristic length scale, a, specify the sample. By transforming a problem of profile-model-matching to the spherical domain, the two parameters are inextricably linked. Modeled profiles determined through forward calculation must contain each. The extrapolation of a specific experimentally determined function $D(T)/a^2$ (e.g., for Durango apatite) to an unstudied specimen possibly of a different grain size may not be accurate.

Does proton irradiation affect helium diffusion kinetics?

An important assumption of the $^4He/^3He$ method is that proton irradiation does not modify the helium diffusion kinetics of the material under investigation. Since the helium

diffusion kinetics is determined on an irradiated sample, it is important to demonstrate whether or not the irradiation modifies a given mineral in such as way as to alter the otherwise natural diffusion kinetics. Our detailed work on Durango apatite demonstrated that ^{4}He diffusivities of irradiated and un-irradiated aliquots are analytically indistinguishable. Figure 5, taken from Shuster et al. (2004), shows that the ^{4}He Arrhenius relationships determined for an irradiated and a non-irradiated aliquot are equivalent. A similar conclusion can be drawn from work on titanite (Shuster et al. 2004). These experiments clearly indicate that for the proton fluence we used, the irradiation does not significantly modify ^{4}He diffusion kinetics. These observations only apply to the dosage and minerals we investigated; experiments on additional minerals at higher fluences could conceivably yield different result.

Diffusive fractionation of helium isotopes?

Due to the ~25% relative difference in mass between ^{3}He and ^{4}He, the potential exists for a difference between the diffusivities of ^{3}He and ^{4}He. For example, from the kinetic theory of gases the ratio of diffusivities for the two isotopes might be expected to be controlled by the inverse square root of their masses, $D^{4He}/D^{3He} = 0.868$. Shown in Figure 6, detailed experiments on Durango apatite clearly indicate far smaller, possibly zero, isotopic mass fractionation in that sample (Shuster et al. 2004). However results on other apatites (unpublished, see below for examples) hint at some degree of fractionation. Thus it is presently unclear whether isotopic mass fractionation does or does not accompany helium release from apatite in all cases. Hence we evaluate its potential effects in this section.

A difference of ≤15% in diffusivity would introduce negligible bias to thermochronometric calculations. However, it would fractionate ^{4}He/^{3}He ratios upon stepwise degassing,

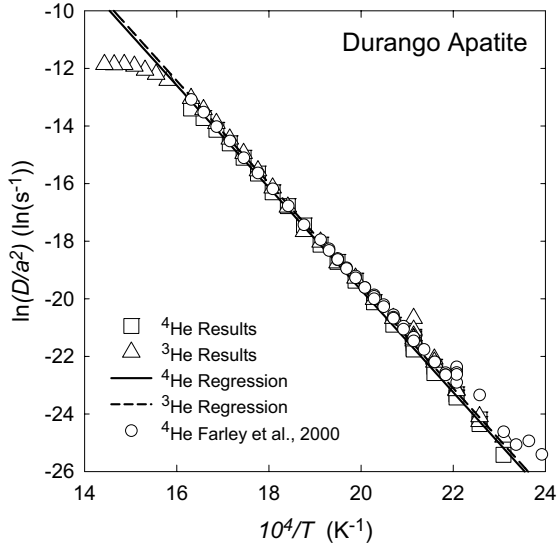

Figure 5. The helium diffusion kinetics of irradiated and non-irradiated Durango apatite, modified from Shuster et al. (2004). Diffusion coefficients (D/a^2) calculated using (Fechtig and Kalbitzer 1966) are plotted against inverse absolute temperature ($10^4/T$). Open triangles are values calculated from proton-induced ^{3}He and open squares calculated from ^{4}He for the irradiated aliquot. The dashed line indicates least squares regression through subsets of the ^{3}He results, and the solid line the ^{4}He results. Shown as open black circles in are ^{4}He results from (Farley 2000) for non-irradiated Durango apatite. Modified from Shuster et al. (2004).

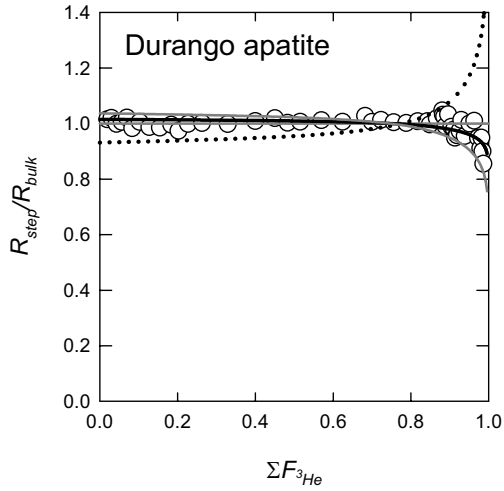

Figure 6. Durango apatite ratio evolution diagram, modified from Shuster et al. (2004). Shown are measured isotope ratios for each release step, R_{step} (R=^{4}He/^{3}He), normalized to the bulk ratio R_{bulk} plotted vs. the cumulative ^{3}He release fraction, $\Sigma F_{^3He}$. Four diffusion models are also shown. The model that best fits the entire dataset, D^{4He}/D^{3He} = 1.03, is shown as a solid black curve with 95% confidence intervals shown as solid gray curves: D^{4He}/D^{3He} = 1.00 and 1.07, respectively. Also shown as a dotted curve is the model corresponding to the inverse root mass relationship: D^{4He}/D^{3He} = SQRT(m_3/m_4) = 0.868. Modified from Shuster et al. (2004).

particularly toward the end of an analysis at high helium yields. Because this would influence the shape of a ^{4}He/^{3}He ratio evolution diagram, the effect needs to be considered when deriving a thermochronometric interpretation.

During sequential degassing, an isotopic difference in diffusivity has a predictable effect on measured ^{4}He/^{3}He ratios. Figure 7 illustrates how this would influence the ^{4}He/^{3}He observations for a typical ^{4}He distribution. For reference, this simulation uses the same ^{4}He profile calculated according to a relatively rapid cooling trajectory as in example 2 (see below). Shown are the resultant ratio evolution spectra for three values of the ratio D^{4He}/D^{3He} between 1.00 and 0.868. Notice that the differences between the curves are small when $\Sigma F_{^3He} < 0.25$ and that all three curves are convergent as $\Sigma F_{^3He}$ approaches ~ 0.8. The curves then strongly diverge at values of $\Sigma F_{^3He} > 0.8$. The differences between the curves are most pronounced as $\Sigma F_{^3He}$ approaches 1.0. This "distillation" effect is due to preferential diffusion of ^{3}He from the domain over the course of the analysis. As expected, the effect is much less pronounced at the beginning of the analysis. Particularly for samples containing a diffusive ^{4}He profile, the spectral shapes for $\Sigma F_{^3He} < 0.25$ are not strongly dependent on the diffusivity ratio.

Because the diffusivity ratio does not appear to be consistent between different samples, its uncertainty will propagate into the *t-T* paths constrained by a ratio evolution diagram. As shown in Shuster and Farley (2004), most of the information on *t-T* is expressed in the ratio evolution for $0 < \Sigma F_{^3He} < 0.25$. Even if a conservative range in D^{4He}/D^{3He} is assumed (e.g., from 1.00 to 0.868), the resultant *t-T* uncertainty will be negligible when models are primarily matched to data below $\Sigma F_{^3He} < 0.25$. Conversely, the ^{4}He/^{3}He ratios as $\Sigma F_{^3He}$ values approach 1.0 are more strongly dependent upon the diffusivity ratio than on the ^{4}He distribution or its corresponding *t-T* path. Systematically increasing ratios towards the end of an analysis likely indicate higher ^{3}He diffusivity compared to ^{4}He in a particular sample. Only when models are matched over the entire range of $\Sigma F_{^3He}$ should the influence of diffusive fractionation become strongly relevant.

Non-uniform U and Th distributions

Throughout this chapter, we have assumed a uniform distribution of U and Th throughout the diffusion domain. A strongly heterogeneous distribution of parent nuclides would clearly influence the final spatial distribution of ^{4}He within a particular sample. Recent efforts on zircon involving laser ablation mass spectrometry have attempted to quantify heterogeneous

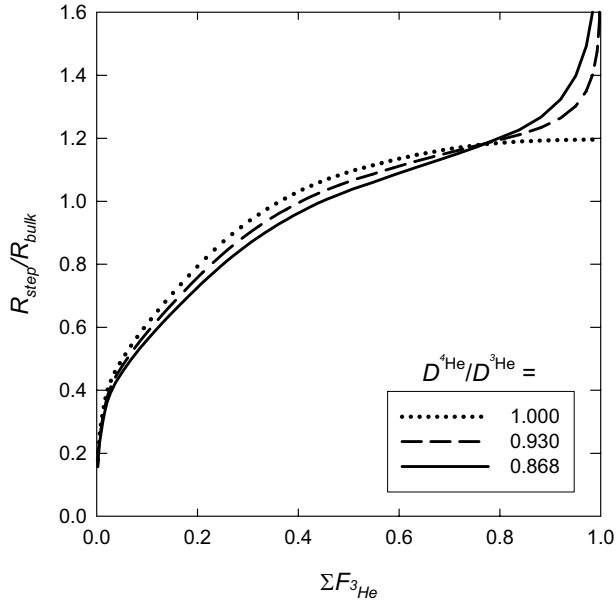

Figure 7. The potential effect of diffusive isotope fractionation upon a ratio evolution diagram. Shown are three $^4He/^3He$ ratio evolution spectra for a common ^4He profile, but for different values of the diffusivity ratio D^{4He}/D^{3He}: 1.00, 0.93 and 0.868. For reference, the ^4He profile was calculated according to the solid black *t-T* path shown in Figure 9(c) and $F_T = 0.81$.

distributions of U and Th on a small spatial scale (Hourigan et al. 2003). If this information is accurately determined for a given sample, it could be easily incorporated into the $^4He/^3He$ method by simply allowing for spatial variability in the ^4He production function. The model ^4He distributions and their corresponding $^4He/^3He$ spectra described in this chapter can easily be calculated for any radially symmetric, but variable ^4He production function.

EXAMPLE APPLICATIONS

In this section we present three example applications of $^4He/^3He$ thermochronometry. These examples are intended to illustrate the quality of $^4He/^3He$ data and *t-T* information that is obtainable using the method rather than to address a particular geological problem. Therefore, the examples are presented without geologic context. The first example is a set of three controlled experiments designed to test the method's accuracy. The other two examples are granitic apatites expected to contain naturally diffusive ^4He distributions which reflect their cooling trajectories. All of these apatites were irradiated simultaneously using a 220 MeV proton beam and total proton fluence of $\sim 1 \times 10^{16}$ protons/cm^2.

Example 1: controlled ^4He distributions

Three aliquots of Durango apatite were heated under vacuum for different durations in order to generate distinct distributions of ^4He. These experiments were performed on the same interior aliquot of Durango apatite used in previous studies (Farley 2000; Shuster et al. 2004) and which had a uniform distribution of ^4He prior to heating. Since the initial ^4He distribution and helium diffusion kinetics of this sample are sufficiently well known, the three aliquots could be partially degassed for different durations to generate diffusive profiles with known

deficit gas fractions (*dgf*). The heated aliquots are analogous to samples which experienced simple, yet known thermal perturbations. Following partial ^{4}He degassing, the aliquots were subjected to proton bombardment and the ^{4}He/^{3}He analysis described above.

The results are shown in Figures 8a-c as ratio evolution spectra. All three diagrams clearly reveal diffusive ^{4}He profiles; each has an initial ^{4}He/^{3}He ratio ~ 0 followed by a systematic increase in ^{4}He/^{3}He to relatively constant values near $R_{step}/R_{bulk} = 1$ when $\Sigma F_{^3He} > 4.0$. It is also clear that each profile is distinct from the others, with the magnitude of diffusive rounding increasing in the order a < b < c. For reference, compare these three results with Figure 6, which shows the observed ^{4}He/^{3}He spectrum for an aliquot containing a uniform ^{4}He distribution within Durango apatite.

Superimposed on each result in Figure 8 is a model ^{4}He/^{3}He spectrum for a diffusive ^{4}He profile within a spherical domain. The models use $D^{4He}/D^{3He} = 1$, and each model corresponds to the specific deficit gas fraction (*dgf*) independently measured on each aliquot. We find excellent agreement between the models and the ^{4}He/^{3}He observations. Although not shown, the ^{3}He Arrhenius plots for each experiment yield diffusion parameters that are statistically indistinguishable from the known helium diffusion kinetics of Durango apatite. Coupled with the deficit gas fractions implied by each ratio evolution spectrum, the ^{3}He based diffusion kinetics successfully constrains the actual heating temperatures and durations which were used to partially degas the ^{4}He distributions prior to irradiation.

These experiments demonstrate that (i) the ratio evolution diagrams successfully recover the expected ^{4}He profiles resulting from simple diffusive modification, (ii) $\ln(D/a^2)$ values calculated from proton-induced ^{3}He adequately describe helium diffusion kinetics in the irradiated sample, and (iii) when combined, this information successfully constrains the actual thermal perturbation experienced by each of the

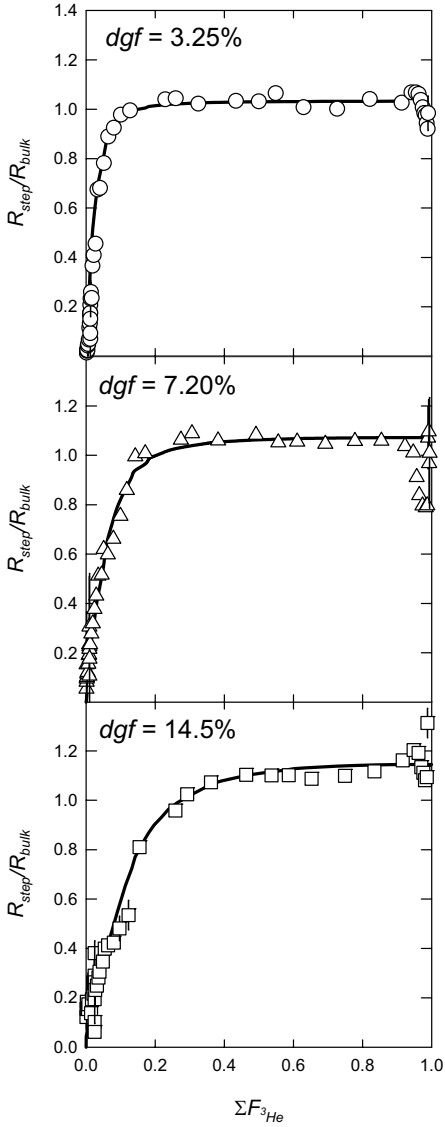

Figure 8. Example 1: Controlled degassing experiments. Shown as points in (a)-(c) are the observed ^{4}He/^{3}He evolution spectra of 3 partially degassed aliquots of Durango apatite. Shown as solid curves are the ^{4}He/^{3}He evolution spectra corresponding to the expected ^{4}He profiles in these aliquots. The deficit gas fractions (*dgf*) of the curves are indicated on the figures.

three aliquots. Because the grains used were not radially symmetric spheres, these results also illustrate the self-consistency of the spherical model. As long as the domain geometry and diffusion coefficients are self-consistently applied, the profiles obtained by forward model matching can be used to constrain a sample's low-temperature thermal history in nature even if the sample is not spherical.

Example 2: natural apatite

The second example is a population of nine euhedral apatites free of inclusions collected from a single hand specimen of a granitic pluton. The apatites had an average F_T value of 0.81 and an α-ejection corrected bulk He age of ~39 ± 2 Ma. Grain-to-grain variance in F_T was ± 0.02. The apatites were subjected to proton bombardment as a larger population of grains, and then subsequently picked for $^4He/^3He$ analysis. The results are shown in Figure 9.

Figure 9a shows the diffusion coefficients determined from ^3He which yields an Arrhenius relationship with activation energy = 135 kJ/mol and $\ln(D_0/a^2)$ = 12.4. These parameters correspond to a 10 °C/Myr helium closure temperature of ~70 °C. Note that 8 points which clearly deviate from linearity at the highest temperatures express the same phenomenon observed by (Farley 2000), and were excluded from the regression. The observed ratio evolution spectrum is shown in Figure 9b as points. Details of the spectrum on

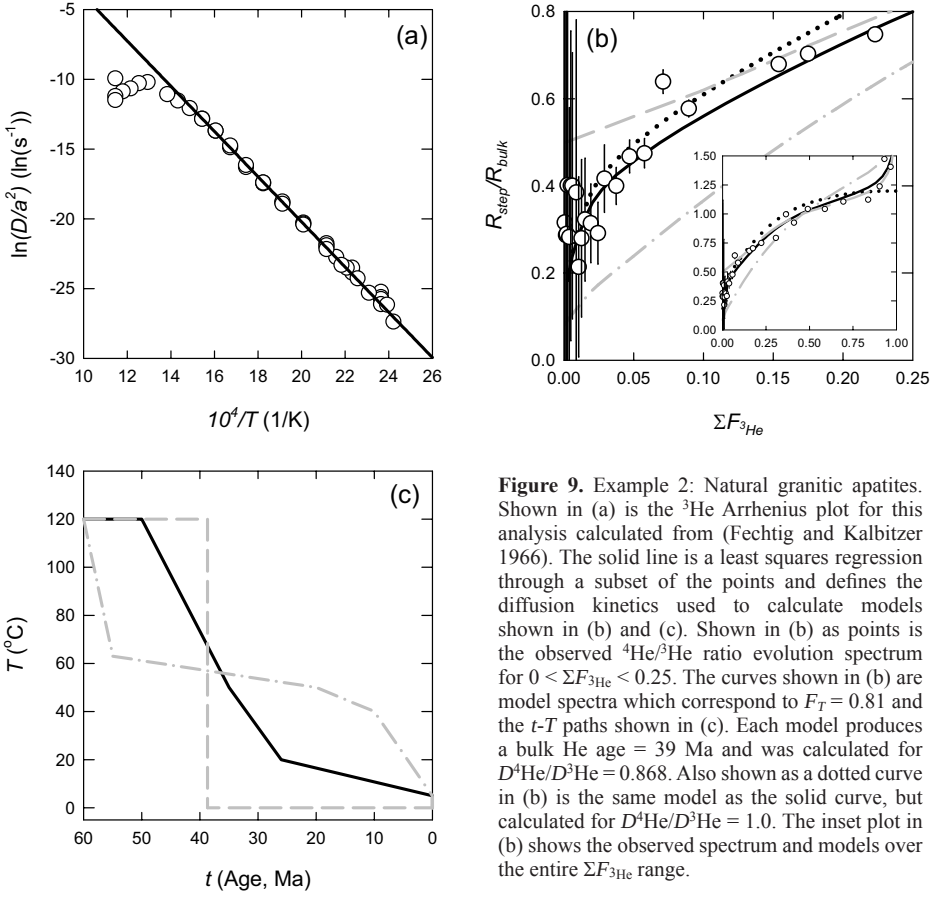

Figure 9. Example 2: Natural granitic apatites. Shown in (a) is the ^3He Arrhenius plot for this analysis calculated from (Fechtig and Kalbitzer 1966). The solid line is a least squares regression through a subset of the points and defines the diffusion kinetics used to calculate models shown in (b) and (c). Shown in (b) as points is the observed $^4He/^3He$ ratio evolution spectrum for $0 < \Sigma F_{^3He} < 0.25$. The curves shown in (b) are model spectra which correspond to $F_T = 0.81$ and the *t*-*T* paths shown in (c). Each model produces a bulk He age = 39 Ma and was calculated for $D^4He/D^3He = 0.868$. Also shown as a dotted curve in (b) is the same model as the solid curve, but calculated for $D^4He/D^3He = 1.0$. The inset plot in (b) shows the observed spectrum and models over the entire $\Sigma F_{^3He}$ range.

$0 < \Sigma F_{3He} < 0.25$ are presented, and the entire spectrum is shown in the inset. The analytical uncertainty indicated in Figure 9b was typically dominated by ^{4}He blank corrections.

Superimposed on Figure 9b are three model ^{4}He/^{3}He spectra calculated for spherical domains with $F_T = 0.81$ and include the effect of α-ejection. Each model shown as a solid or dashed curve corresponds to a cooling trajectory shown in Figure 9c and spatial ^{4}He distribution which would result in the bulk He age of the sample, 39 Ma. The three models were calculated for $D^{4He}/D^{3He} = 0.868$; notice in the inset that elevated ^{4}He/^{3}He ratios when $\Sigma F_{3He} > 0.80$ hint at diffusive fractionation between proton-induced ^{3}He and radiogenic ^{4}He in this sample. For comparison, the same model shown as a solid black curve is also shown for $D^{4He}/D^{3He} = 1.0$ as a dotted black curve.

The three cooling models clearly do not represent an exhaustive coverage of cooling history space, but are simply intended to illustrate the types of models which can be developed for ^{4}He/^{3}He comparison. The initially observed ^{4}He/^{3}He ratios with value ~ 0.3 require that the sample had accumulated a significant fraction of its ^{4}He below ~30 °C. This and the observed curvature when $\Sigma F_{3He} < 0.25$ clearly eliminate the two models shown as dashed curves as possible *t-T* paths for the sample. Instant cooling at 39 Ma would result in initial ^{4}He/^{3}He ratios ~ 0.55, and prolonged residence in the partial retention zone would result in a more diffusive distribution. The data are reasonably consistent with the model shown as a solid black curve corresponding to relatively rapid cooling before 25 Ma, followed by more gradual recent cooling below 30 °C. Note that models calculated for $D^{4He}/D^{3He} = 1.0$ would yield a very similar result, particularly when matching observations between $0 < \Sigma F_{3He} < 0.25$.

Example 3: natural apatite

The third example is a population of 27 apatites collected from a hand specimen of a different granitic pluton. These apatites were also free of inclusions and euhedral with an average F_T value of 0.76 and an α-ejection corrected bulk He age of ~9.7 ± 0.6 Ma. Grain-to-grain variance in F_T was ± 0.03. The apatites were also subjected to proton bombardment as a larger population of grains, and then subsequently selected for ^{4}He/^{3}He analysis. The results are shown in Figure 10.

Diffusion coefficients calculated from ^{3}He are shown in Figure 10a. The best fit Arrhenius relationship (which excludes the 7 highest temperature steps for the same reason as discussed above) is shown as a solid line in Figure 10a and corresponds to an activation energy of 124 kJ/mol and $\ln(D_0/a^2) = 10.2$. These apatites are slightly less helium retentive than the previous example, with a 10 °C/Myr helium closure temperature of ~60 °C. Details of the ^{4}He/^{3}He spectrum are shown in Figure 10b for $\Sigma F_{3He} < 0.25$, and the entire spectrum is shown in the inset. The analytical uncertainties were typically dominated by ^{4}He blank corrections.

As seen in Figure 10b, the ^{4}He/^{3}He ratios measured between $0.05 < \Sigma F_{3He} < 0.25$ were very well constrained and show systematically increasing values. Superimposed on the data are three models corresponding to the cooling trajectories shown in Figure 10c. Each model uses the Arrhenius relationship shown in Figure 10a, and each corresponds to a bulk He age of 9.7 Ma. Sharply increasing ratios for $\Sigma F_{3He} > 0.80$ (Fig. 10b inset) suggest diffusive fractionation of the helium isotopes; the three models were calculated for $D^{4He}/D^{3He} = 0.868$. As with the previous example, the ^{4}He/^{3}He data are not consistent with either immediate cooling at the He age or prolonged residence at elevated temperatures of partial ^{4}He retention. The initially elevated ^{4}He/^{3}He ratios near the grains' edges require that a significant fraction of ^{4}He was accumulated at relatively low temperatures. The data are in excellent agreement with a thermal history involving ~15 °C/Myr cooling to < 30°C by ~ 6 Ma (solid black curve). Interestingly, the mean value $R_{initial}/R_{bulk} = 0.3$ corresponds to an "edge age" ~ 5.5 Ma for this sample, which is in good agreement with the full model calculation.

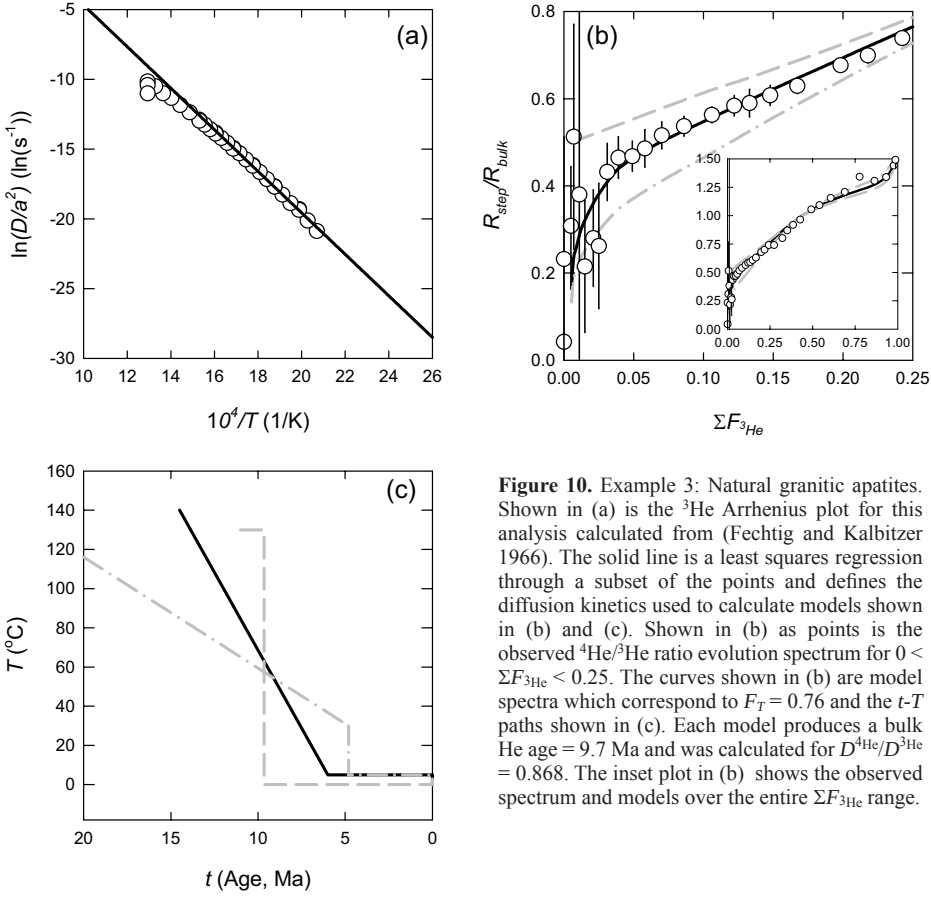

Figure 10. Example 3: Natural granitic apatites. Shown in (a) is the ^{3}He Arrhenius plot for this analysis calculated from (Fechtig and Kalbitzer 1966). The solid line is a least squares regression through a subset of the points and defines the diffusion kinetics used to calculate models shown in (b) and (c). Shown in (b) as points is the observed ^{4}He/^{3}He ratio evolution spectrum for $0 < \Sigma F_{^3He} < 0.25$. The curves shown in (b) are model spectra which correspond to $F_T = 0.76$ and the *t-T* paths shown in (c). Each model produces a bulk He age = 9.7 Ma and was calculated for $D^{4He}/D^{3He} = 0.868$. The inset plot in (b) shows the observed spectrum and models over the entire $\Sigma F_{^3He}$ range.

Although the successful models shown in examples 2 and 3 (solid curves Figs. 9b and 10b) do not prove the *t-T* paths of the samples, the ^{4}He/^{3}He observations clearly permit elimination of many possible thermal histories in a very low temperature range. The examples illustrate that high-precision ^{4}He/^{3}He data is attainable on relatively small populations of apatites, and that when combined with the bulk He age, these data can be used to place stringent restrictions on the low temperature *t-T* paths of the samples.

CONCLUSIONS

A uniform ^{3}He distribution can be artificially produced within minerals by irradiation with a 220 MeV proton beam. Outgassing of spallation ^{3}He produced by such irradiation can be used as a proxy for radiogenic ^{4}He diffusion. The ability to generate a uniform ^{3}He distribution within minerals permits helium diffusivity measurements on samples in which the natural concentration distribution is non-uniform. Variations in the ^{4}He/^{3}He ratio over the course of a stepwise heating experiment reflect the initial ^{4}He distribution within the sample. Both forward and inverse modeling can be used to constrain these profiles, which can in turn be used to constrain the *t-T* path of the sample. When coupled with the bulk (U-Th)/He age of

a sample, this information places stringent limitations on the possible low temperature thermal histories of a particular sample.

ACKNOWLEDGMENTS

We thank D. Burnett and J. Sisterson for helpful discussions and F. Albarède for a helpful review of the manuscript. This work was supported by the National Science Foundation and by a N.S.F. Graduate Research Fellowship to D.L.S.

REFERENCES

Albarède F (1978) The recovery of spatial isotope distributions from stepwise degassing data. Earth Planet Sci Lett 39(3):387-397

Carslaw HS, Jaeger JC (1959) Conduction of Heat in Solids. Oxford University Press, New York

Crank J (1975) The Mathematics of Diffusion. Oxford University Press, New York

Dodson MH (1973) Closure temperatures in cooling geological and petrological systems. *Contrib Mineral Petrol* 40:259-274

Farley K, Reiners P, Nenow V (1999) An apparatus for high-precision helium diffusion measurements from minerals. Anal Chem 71:2059-2061

Farley KA (2000) Helium diffusion from apatite: general behavior as illustrated by Durango fluorapatite. J Geophys Res 105:2903-2914

Farley KA (2002) (U-Th)/He dating: techniques, calibrations, and applications. Rev Mineral Geochem 47: 819-844

Farley KA, Wolf RA, Silver LT (1996) The effects of long alpha-stopping distances on (U-Th)/He ages. Geochim Cosmochim Acta 60:4223-4229

Fechtig H, Kalbitzer S (1966) The diffusion of argon in potassium bearing solids. *In:* Potassium-Argon Dating. Schaeffer OA, Zahringer J (eds) Springer, Heidelberg, p 68-106

Gallagher K (1995) Evolving temperature histories from apatite fission-track data. Earth Planet Sci Lett 136: 421-435

Harrison TM, Grove M, Lovera OM, Zeitler PK (2005) Continuous thermal histories from inversion of closure profiles. Rev Mineral Geochem 58:389-409

Hodges K, Boyce J (2003) Laser-ablation (U-Th)/He geochronology. Eos Trans AGU, Fall Meet Suppl 84(46)

Hourigan JK, Reiners PW, Nicolescu S, Plank T, Kelley K (2003) Zonation-dependent α-ejection correction by laser ablation ICP-MS depth profiling: toward improved precision and accuracy of (U-Th)/He ages. Eos Trans AGU, Fall Meet Suppl 84(46)

House MA, Wernicke BP, Farley KA (1998) Dating topography of the Sierra Nevada, California, using apatite (U-Th)/He ages. Nature 396:66-69

Leya I, Busemann H, Baur H, Wieler R, Gloris M, Neumann S, Michel R, Sudbrock F, Herpers U (1998) Cross sections for the proton-induced production of He and Ne isotopes from magnesium, aluminum, and silicon. Nucl Instr Methods Phys Res B 145:449-458

Leya I, Lange HJ, Neumann S, Wieler R, Michel R (2000) The production of cosmogenic nuclides in stony meteoroids by galactic cosmic-ray particles. Meteor Planet Sci 35(2):259-286

Lippolt HJ, Leitz M, Wernicke RS, Hagedorn B (1994) (U+Th)/He dating of apatite: experience with samples from different geochemical environments. Chem Geol 112:179-191

Lovera O, Richter F, Harrison T (1989) The $^{40}Ar/^{39}Ar$ thermochronometry for slowly cooled samples having a distribution of diffusion domain sizes. J Geophys Res 94:17917-17935

McDougall I, Harrison TM (1999) Geochronology and Thermochronology by the $^{40}Ar/^{39}Ar$ method. Oxford University Press, New York

Meesters AGCA, Dunai TJ (2002a) Solving the production-diffusion equation for finite diffusion domains of various shapes (part I): implications for low-temperature (U-Th)/He thermochronology. Chem Geol 186: 333-344

Meesters AGCA, Dunai TJ (2002b) Solving the production-diffusion equation for finite diffusion domains of various shapes (part II): application to cases with α-ejection and non-homogeneous distribution of the source. Chem Geol 186:347-363

Reiners PW, Farley KA (1999) Helium diffusion and (U-Th)/He thermochronometry of titanite. Geochim Cosmochim Acta 63:3845-3859

Reiners PW, Farley KA (2001) Influence of crystal size on apatite (U-Th)/He thermochronology: an example from the Bighorn mountains, Wyoming. Earth Planet Sci Lett 188:413-420
Reiners PW, Farley KA, Hickes HJ (2002) He diffusion and (U-Th)/He thermochronometry of zircon: Initial results from Fish Canyon Tuff and Gold Butte, Nevada. Tectonophys 349:297-308
Reiners PW, Spell TL, Nicolescu S, Zanetti KA (2004) Zircon (U-Th)/He thermochronometry: He diffusion and comparisons with Ar-40/Ar-39 dating. Geochim Cosmochim Acta 68(8):1857-1887
Shuster DL, Farley KA (2004) $^{3}He/^{4}He$ thermochronometry. Earth Planet Sci Lett 217(1-2):1-17
Shuster DL, Farley KA, Sisterson JM, Burnett DS (2004) Quantifying the diffusion kinetics and spatial distributions of radiogenic ^{4}He in minerals containing proton-induced ^{3}He. Earth Planet Sci Lett 217(1-2):19-32
Stockli DF, Farley KA, Dumitru TA (2000) Calibration of the (U-Th)/He thermochronometer on an exhumed fault block, White Mountains, California. Geology 28:983-986
Turner G (1969) Thermal histories of meteorites by the $^{40}Ar/^{39}Ar$ method. *In:* Meteorite Research. Millman PM (ed) Reidel, Dordrecht, p 407-417
Warnock AC, Zeitler PK, Wolf RA, Bergman SC (1997) An evaluation of low-temperature apatite U-Th/He thermochronometry. Geochim Cosmochim Acta 61(24):5371-5377
Wieler R (2002) Cosmic-ray-produces noble gases in meteorites. Rev Mineral Geochem 47:125-163
Wolf RA, Farley KA, Silver LT (1996) Helium diffusion and low-temperature thermochronometry of apatite. Geochim Cosmochim Acta 60(21):4231-4240